Supplementary Information for

Shifts in MJO Behavior Enhance Predictability of Subseasonal Weather Whiplashes

Tat Fan Cheng[1,2], Bin Wang[2,3]*, Fei Liu[4,5,6], Guosen Chen[7], and Mengqian Lu[1]

[1] Department of Civil and -Environmental Engineering, The Hong Kong University of Science and Technology, Clear Water Bay, Hong Kong, China

[2] International Pacific Research Center, University of Hawai'i at Mānoa, Honolulu, HI, USA

[3] Department of Atmospheric Sciences, University of Hawai'i at Mānoa, Honolulu, HI, USA

[4] School of Atmospheric Sciences, Sun Yat-Sen University, Zhuhai, China

[5] Key Laboratory of Tropical Atmosphere-Ocean System Ministry of Education, Zhuhai, China

[6] Southern Marine Science and Engineering Guangdong Laboratory, Zhuhai, China

[7] Earth System Modeling Center, Key Laboratory of Meteorological Disaster of Ministry of Education, Collaborative Innovation Center on Forecast and Evaluation of Meteorological Disasters, Nanjing University of Information Science and Technology, Nanjing, China

Corresponding author (*): Bin Wang (wangbin@hawaii.edu)

Contents of this file

Supplementary Table 1. The CMIP6 climate model simulations examined in this study. The spatial resolution of the model output is shown in the number of grids.

No.	Model	Institution & Nation	Lon × Lat (in grids)	Realization
1	ACCESS-CM2	Commonwealth Scientific and Industrial Research Organi	192 × 144	r1i1p1f1
2	ACCESS-ESM1-5	sation (CSIRO)-Australian Research Council Centre of Excellence for Climate System Science (ARCCSS), Australia	192 × 145	r1i1p1f1
3	CESM2	National Center for Atmospheric Research (NCAR), USA	288 × 192	r4i1p1f1
4	CMCC-CM2-SR5	Fondazione Centro Euro-Mediterraneo sui Cambiamenti	288 × 192	r1i1p1f1
5	CMCC-ESM2	Climatici (CMCC), Italy	288 × 192	r1i1p1f1
6	CNRM-CM6-1	Centre National de Recherches Meteorologiques-Centre	256 × 128	r1i1p1f2
7	CNRM-CM6-1-HR	Europeen de Recherche et de Formation Avancee en	720 × 360	r1i1p1f2
8	CNRM-ESM2-1	Calcul Scientifique (CNRM-CERFACS), France	256 × 128	r1i1p1f2
9	CanESM5	Canadian Centre for Climate Modelling and Analysis (CCCma), Canada	128 × 64	r1i1p1f1
10	EC-Earth3	EC-Earth-Consortium, European countries	512 × 256	r1i1p1f1
11	EC-Earth3-CC		512 × 256	r1i1p1f1
12	EC-Earth3-Veg		512 × 256	r1i1p1f1
13	EC-Earth3-Veg-LR		320 × 160	r1i1p1f1
14	FGOALS-g3	Chinese Academy of Sciences (CAS), China	180 × 80	r1i1p1f1
15	GFDL-CM4	National Oceanic and Atmospheric Administration-Geophysical Fluid Dynamics Laboratory (NOAA-GFDL), USA	144 × 90	r1i1p1f1
16	GISS-E2-1-G	Goddard Institute for Space Studies (NASA-GISS), USA	144 × 90	r1i1p1f2
17	IITM-ESM	Centre for Climate Change Research, Indian Institute of Tropical Meteorology Pune (CCCR-IITM), India	192 × 94	r1i1p1f1
18	INM-CM4-8	Institute for Numerical Mathematics (INM), Russia	180 × 120	r1i1p1f1
19	INM-CM5-0		180 × 120	r1i1p1f1
20	IPSL-CM6A-LR	Institut Pierre Simon Laplace (IPSL), France	144 × 143	r1i1p1f1
21	MIROC-ES2H	Japan Agency for Marine-Earth Science (JAMSTEC),	256 × 128	r1i1p4f2
22	MIROC-ES2L	Atmosphere and Ocean Research Institute (AORI),	128 × 64	r1i1p1f2
23	MIROC6	National Institute for Environmental Studies (NIES), and RIKEN Center for Computational Science (R-CCS), Japan	256 × 128	r1i1p1f1
24	MPI-ESM1-2-HR	Max Planck Institut fur Meteorologie (MPI), Germany	384 × 192	r1i1p1f1
25	MPI-ESM1-2-LR		192 × 96	r1i1p1f1
26	MRI-ESM2-0	Meteorological Research Institute (MRI), Japan	320 × 160	r1i1p1f1
27	NESM3	Nanjing University of Information Science and Technology (NUIST), China	192 × 96	r1i1p1f1
28	TaiESM1	Research Center for Environmental Changes (AS-RCEC), Taiwan	288 × 192	r1i1p1f1

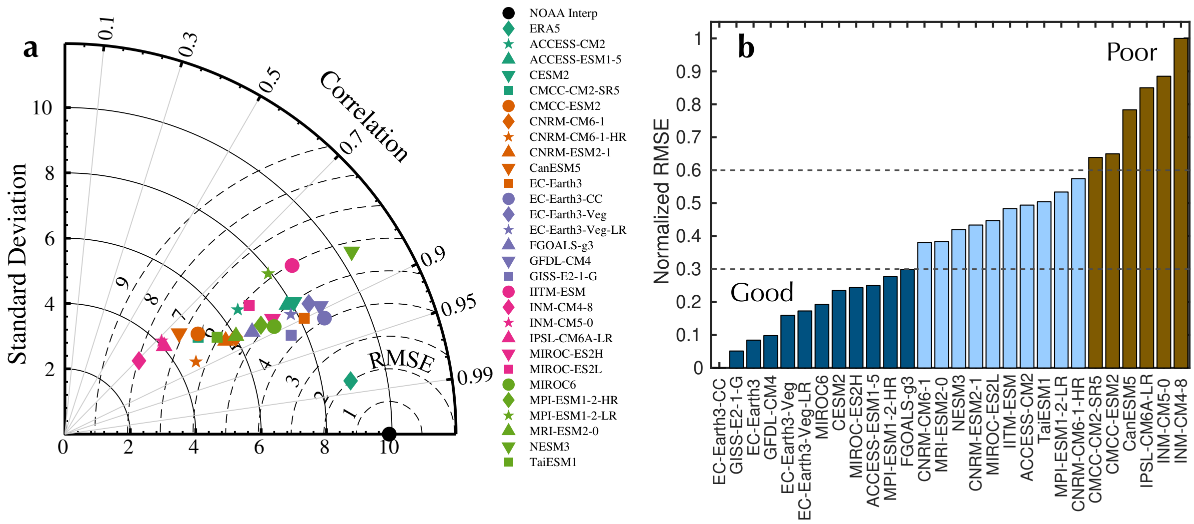

Supplementary Fig. 1. CMIP6 model performance in Madden-Julian Oscillation (MJO) diversity. a, Taylor diagram of the performance of 28 CMIP6 models in reproducing the historical (1979–2014) MJO diversity by matching the composite lag-longitude patterns of 20–70-day outgoing longwave radiation (OLR; units: W m^{-2}) of all four MJO clusters to the corresponding benchmark patterns (see Methods). **b,** CMIP6 models sorted by the normalized root-mean-square-error (RMSE) from the observed MJO diversity. Shading in green highlights the 12 good models with a normalized RMSE of less than 0.3, while shading in red denotes the six poor models with a normalized RMSE of higher than 0.6.

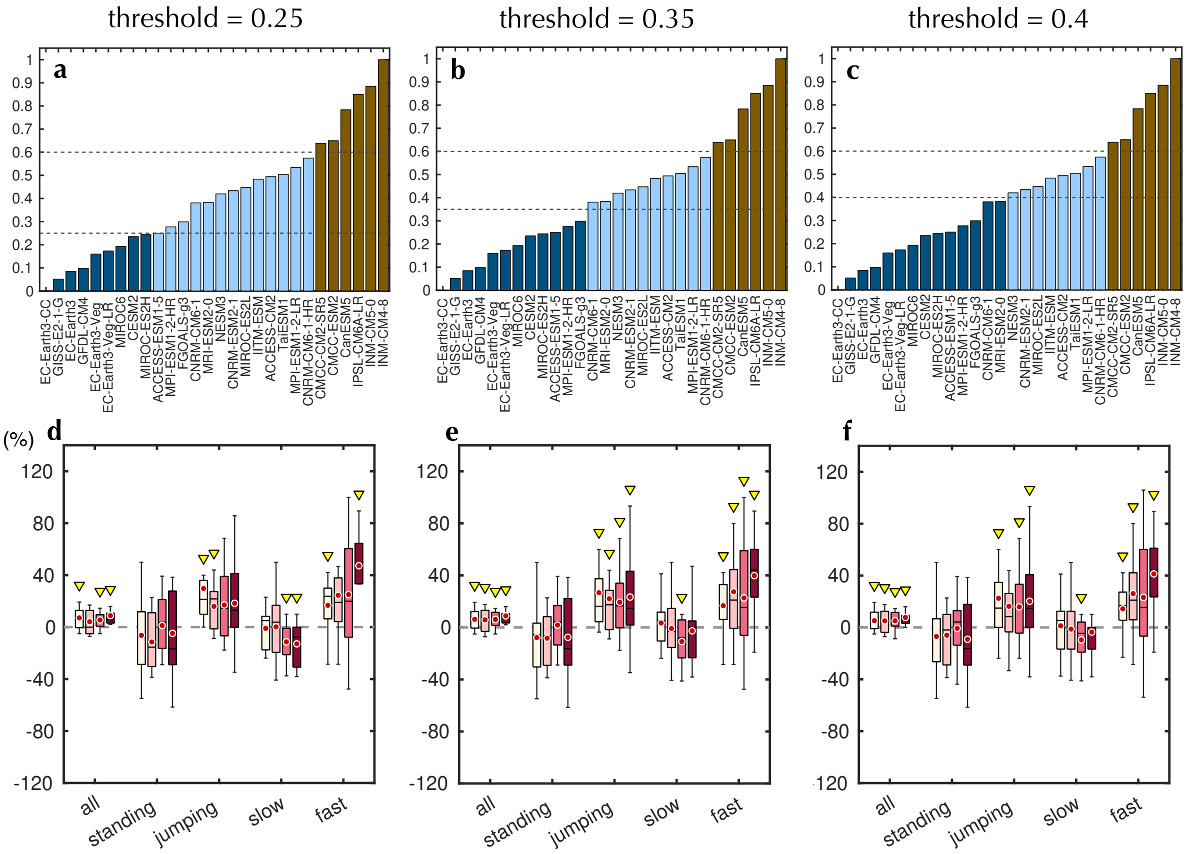

Supplementary Fig. 2. Sensitivity tests on the selection of good models. Similar to Supplementary Fig. 1b, but for the good models (denoted by navy blue bars) based on a threshold of **a,** 0.25, **b,** 0.35, and **c,** 0.4. Note that using a threshold of 0.35 gives the same set of good models as the original threshold, which is 0.3. **d–f,** Similar to Fig. 1b, but based on the three different thresholds.

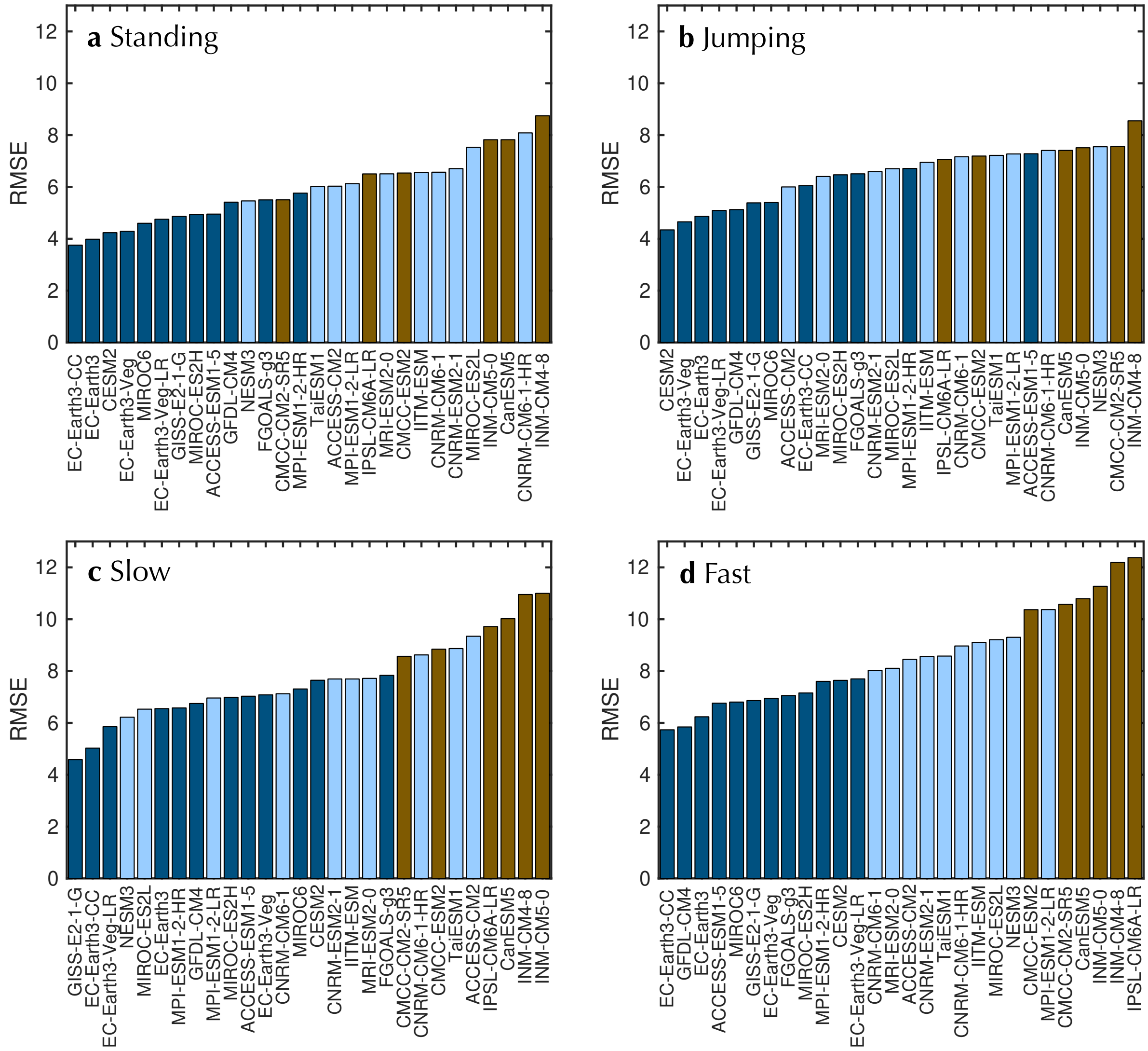

Supplementary Fig. 3. CMIP6 model performance based on individual MJO type. The performance of CMIP6 model in reproducing **a,** standing, **b,** jumping, **c,** slow, and **d,** fast MJO based on RMSE. Bars in navy blue indicate the 12 good models selected based on the original evaluation scheme on the overall performance of all four MJO types, while bars in brown denote the six poor models.

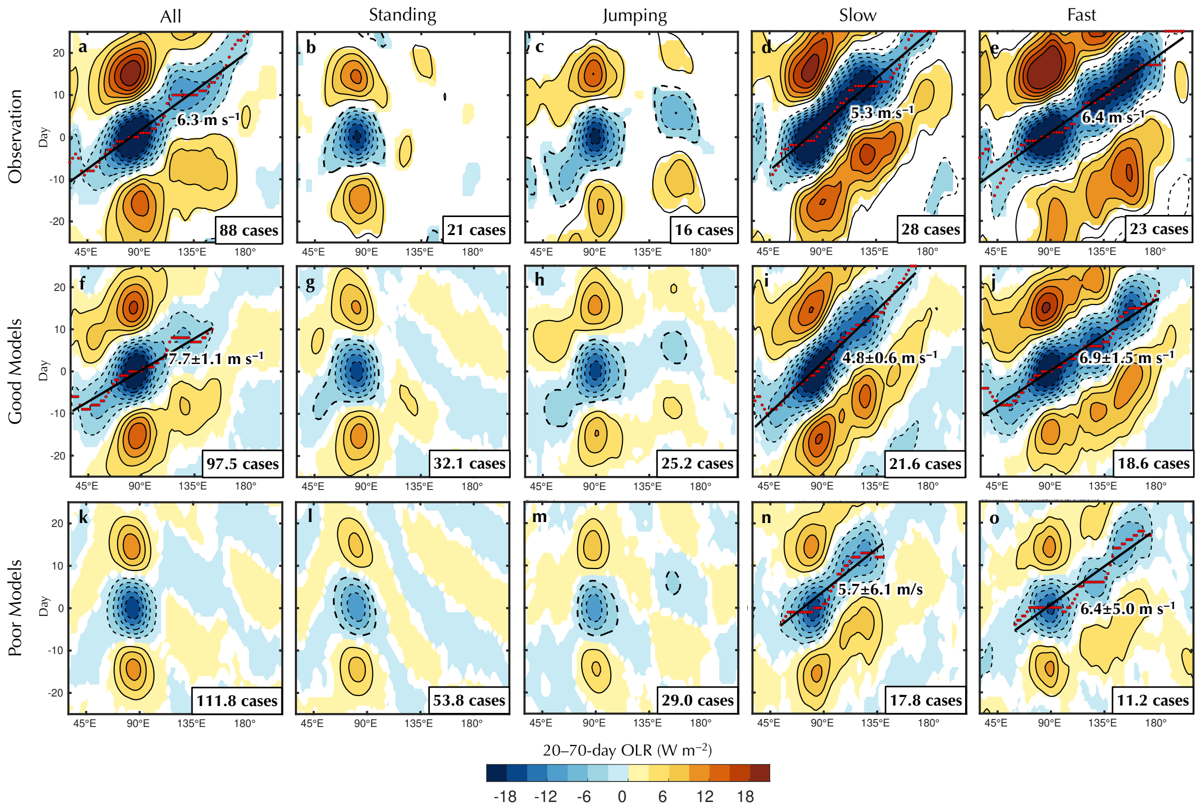

Supplementary Fig. 4. The Madden-Julian Oscillation (MJO) diversity derived from satellite observations and CMIP6 models. a–e, The lag-longitude Hovmöller diagrams of the composited NOAA-interpolated equatorial (10°S–10°N) 20–70-day outgoing longwave radiation (OLR; units: W m^{-2}) for all MJO events and each of the four archetypes over 1979–2014. Only the matched cases with a Silhouette value higher than or equal to 0.06 are considered. Only statistically significant values at the 0.05 level (Student's *t*-test) are shown. The following two rows are similar to panels a–d, but based on the simulations of **f–j,** the 12 good models and **k–o,** the six poor models. The phase speed, with the uncertainty showing inter-model spread (±1 S.D.), is displayed next to the propagating MJO based on a regression approach (see Methods). The minimum OLR points at each longitude of the MJO on which the regression approach was performed are shown in red. The number shown at the bottom right is the case number averaged across the models.

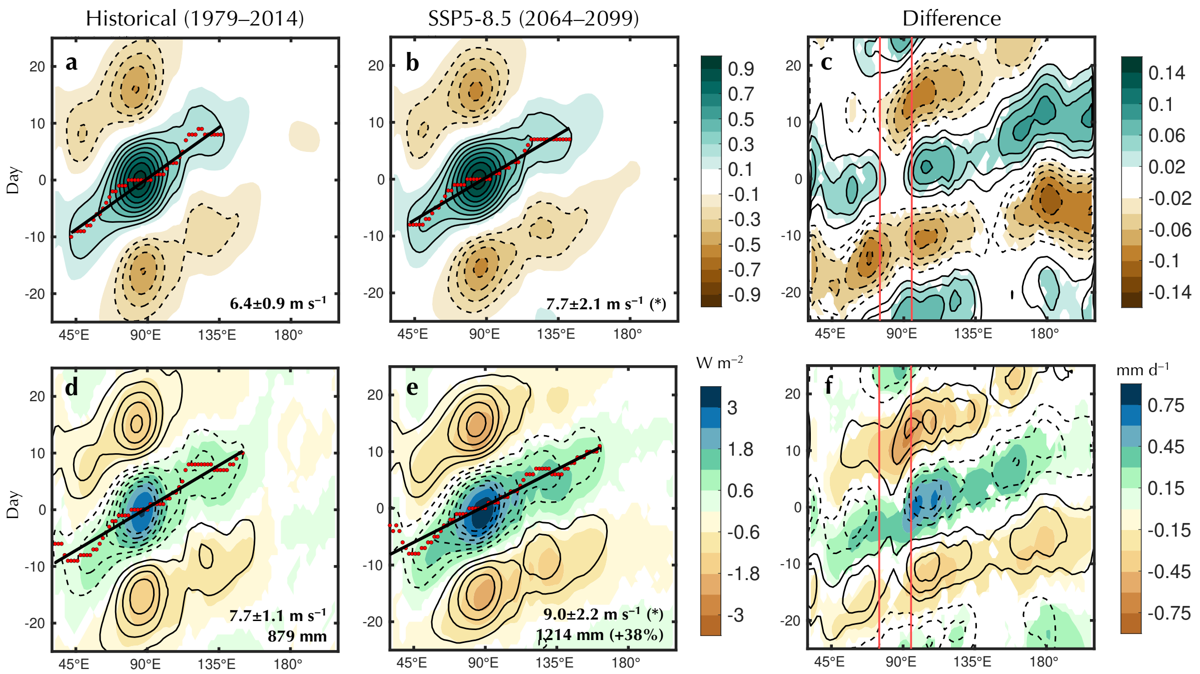

Supplementary Fig. 5. Future changes in the overall MJO propagation and the associated precipitation. Hovmöller diagrams of the lead-lag correlation between the tropical mean (10°S–10°N) 20–70-day OLR anomaly with reference to itself over the equatorial Indian Ocean (EIO; 75°–95°E) during the boreal cold season (November–April) in the **a,** historical (1979–2014) and **b,** far-future (2064–2099) SSP5–8.5 scenarios based on the MME12. The estimated propagation speed is shown in the plot, with the asterisk (*) denoting that the future MJO propagation speeds derived from individual models significantly differ from that in the historical period at the 0.1 level (two-sample Student's *t*-test). **c,** The difference between the two scenarios, with the shading showing the values with the sign agreed by ≥ 66% of the models. The double vertical lines in red mark the longitudinal range (75°–95°E) where the eastern Indian Ocean MJO was identified. **d–f,** The composite mean 20–70-day rainfall anomaly (shading, units: mm day^{-1}) and the OLR anomaly (contours, units: W m^{-2}) based on the identified MJO events over the EIO. The bottom right shows the tropical mean total 20–70-day rainfall accumulation associated with the MJO events.

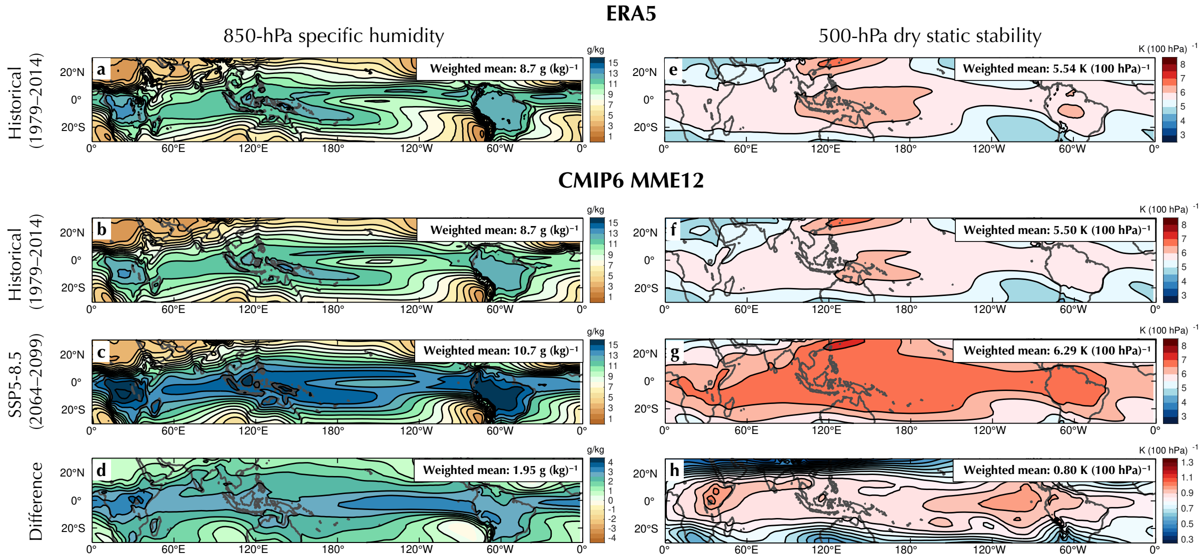

Supplementary Fig. 6. Future changes in the mean-state 850-hPa specific humidity and 500-hPa dry static stability. a Spatial map of the tropical mean (30°S–30°N) background 850-hPa specific humidity (units: g kg^{-1}) during the historical (1979–2014) boreal winter season (November–April) based on ERA5 reanalysis. **b–d,** Similar to panel a, but for the historical (1979–2014) period, the SSP5-8.5 scenarios, and their difference based on the MME12. **e–h,** Similar to panels a–d, but for the 500-hPa dry static stability (units: K (100 hPa)$^{-1}$). The top right shows the area-weighted mean over 30°S–30°N.

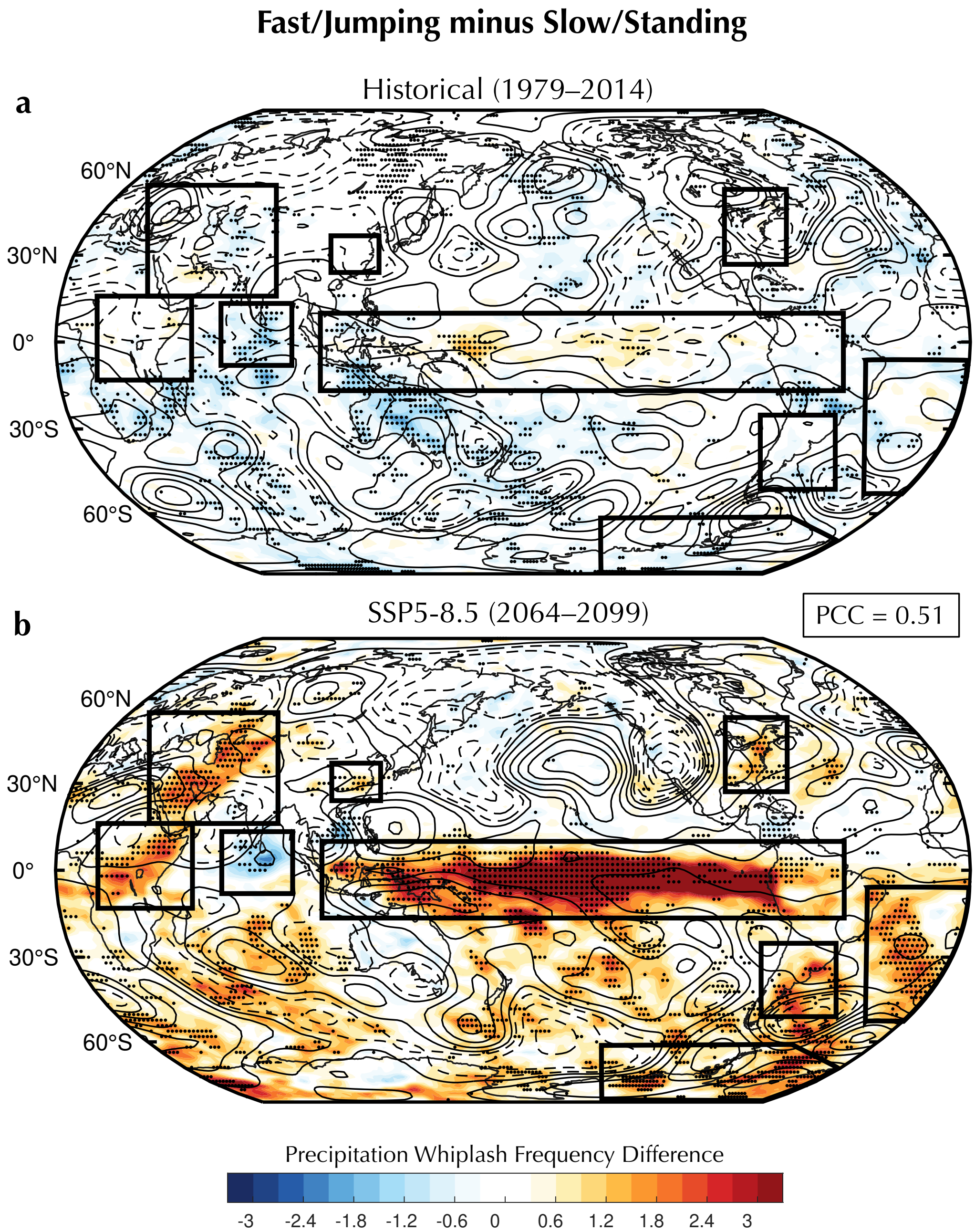

Supplementary Fig. 7. Future shift in the difference in precipitation whiplash frequency and circulation variability between fast/jumping and slow/standing MJOs. Similar to Fig. 3, but without normalizing the precipitation whiplash frequency by the frequency of the four archetypes of MJO events.

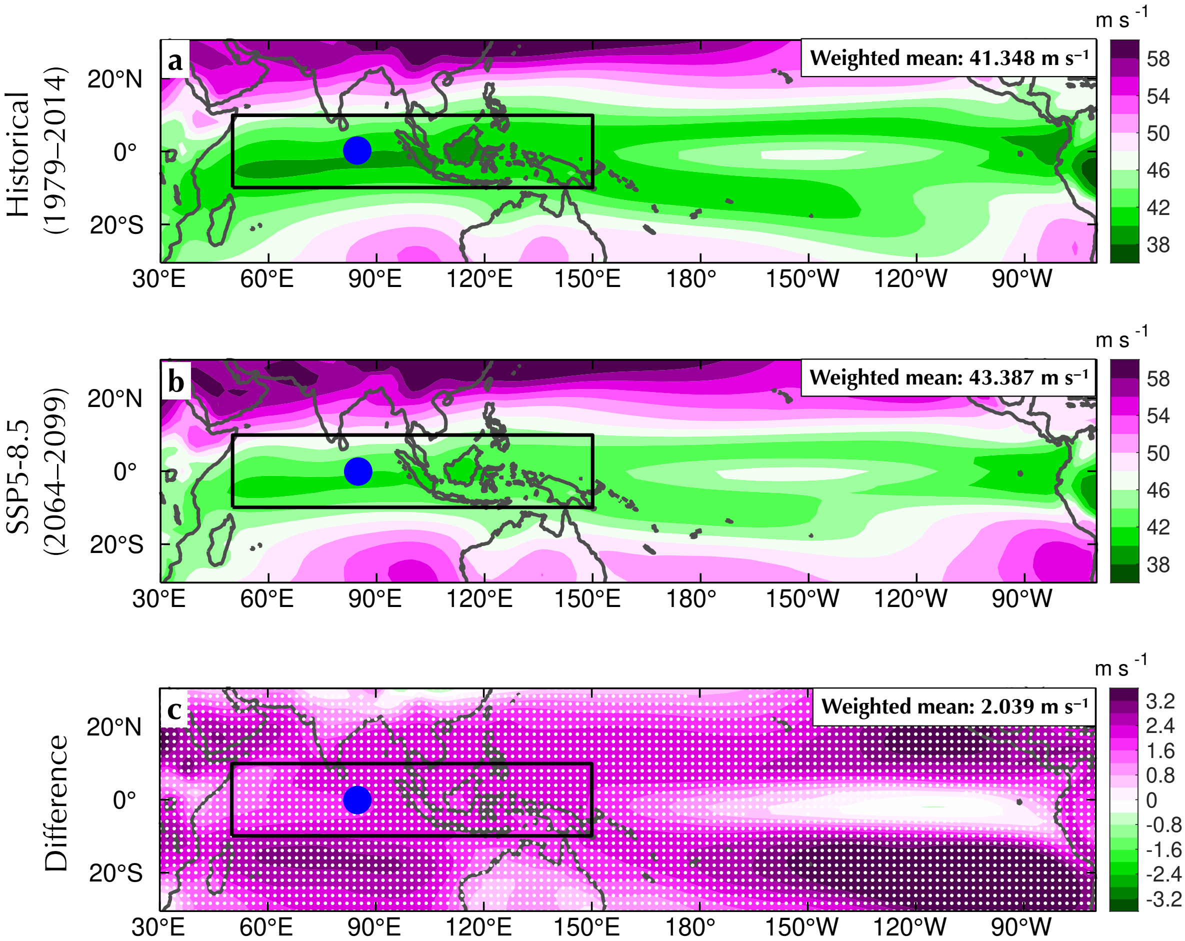

Supplementary Fig. 8. Future changes in the background moist GW wave speed associated with MJO. Composite of the background 3-month running mean moist GW wave speed C_1 (units: m s^{-1}) with the central month being the month of day 0 of each MJO event in **a,** historical run (1979–2014) and **b,** far future SSP5-8.5 run (2064–2099) based on the MME12. **c,** The difference between the two scenarios, with the stippling denoting the values with the sign agreed by ≥ 66% of the models. The top right shows the area-weighted average of C_1 in the vicinity of the MJO (outlined in black).

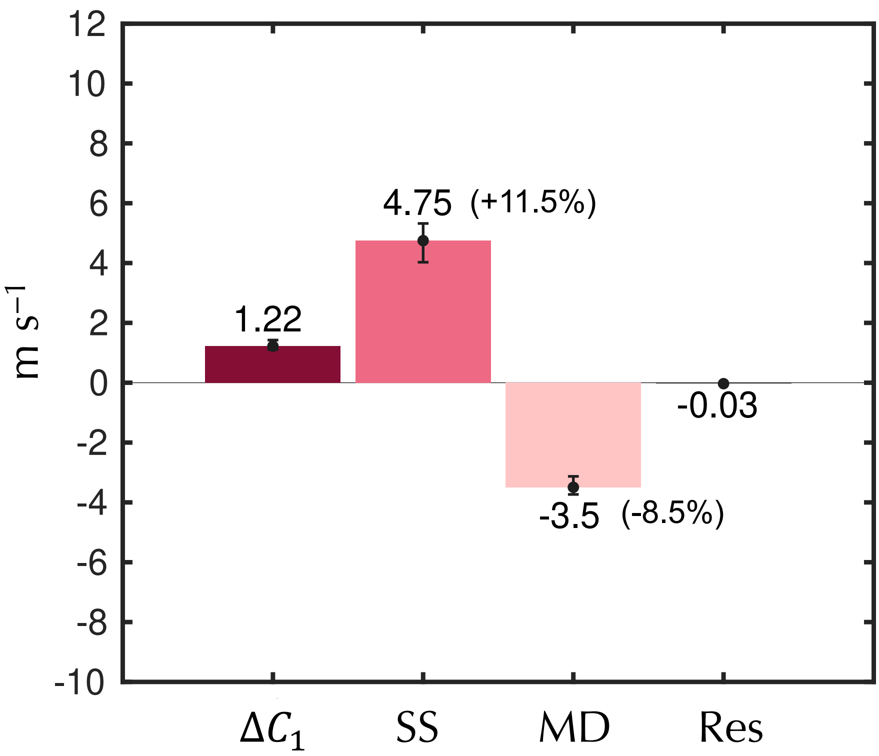

Supplementary Fig. 9. Projected changes in moist GW wave budget under the mitigated scenario. Similar to Fig. 5c, but for the projected changes in SSP2-4.5 scenario (2064–2099) with respect to the historical run (1979–2014).

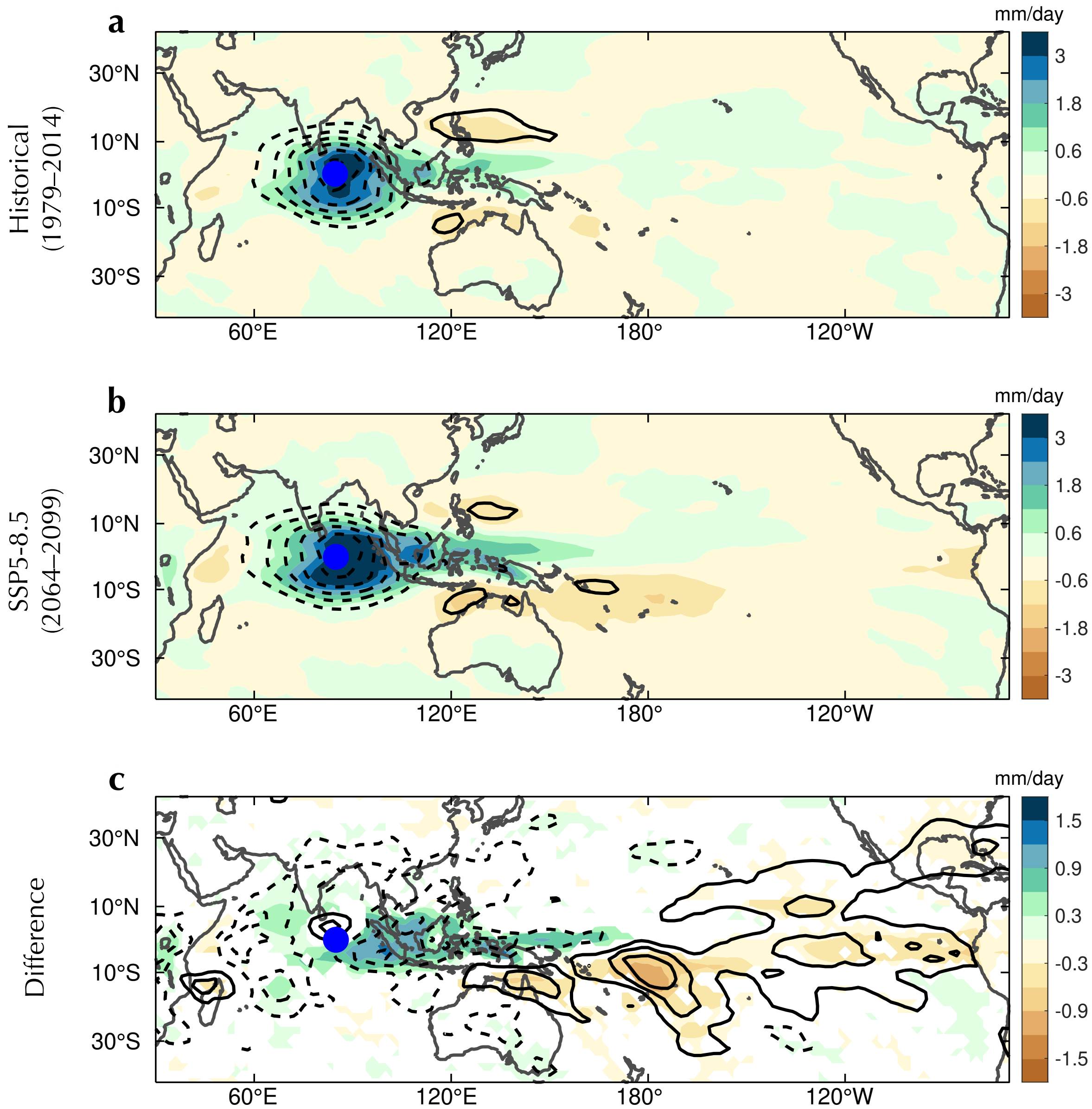

Supplementary Fig. 10. Future changes in the future MJO-coupled convection. Similar to Fig. 4a–c, but for the MJO-associated precipitation (shading, units: mm day^{-1}) and OLR (contour, units: W m^{-2}). The solid (dashed) contours denote positive (negative) values, with an interval of 5 W m^{-2} in panels a and b, and an interval of 1 W m^{-2} in panel c.

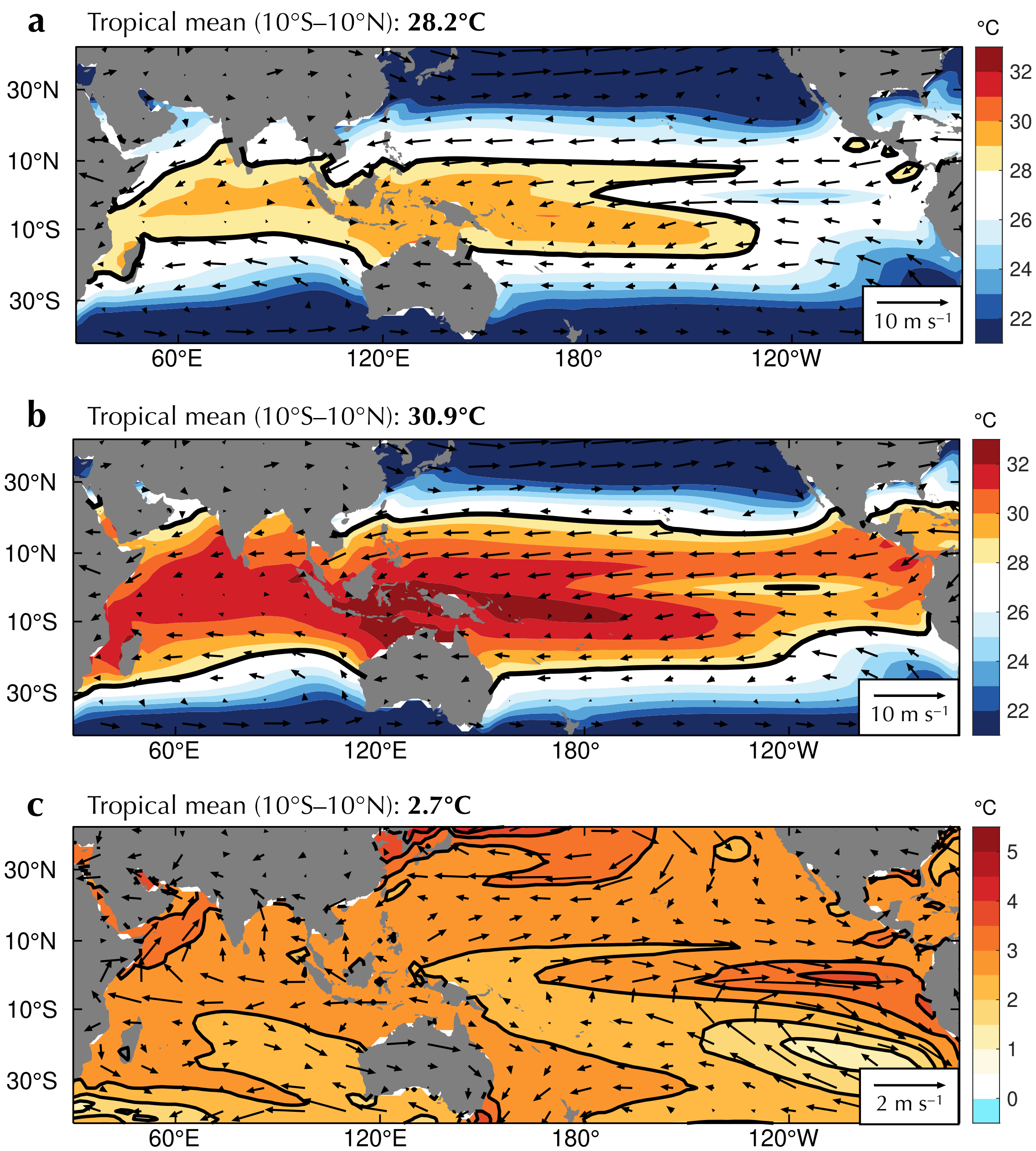

Supplementary Fig. 11. Future changes in the mean-state SST. d–f, Similar to Fig. 4a–c, but for the background 3-month running mean SST (shading) and 850-hPa winds (vectors). The warm pool is outlined based on the 28°C isotherm of SST in panels a and b.

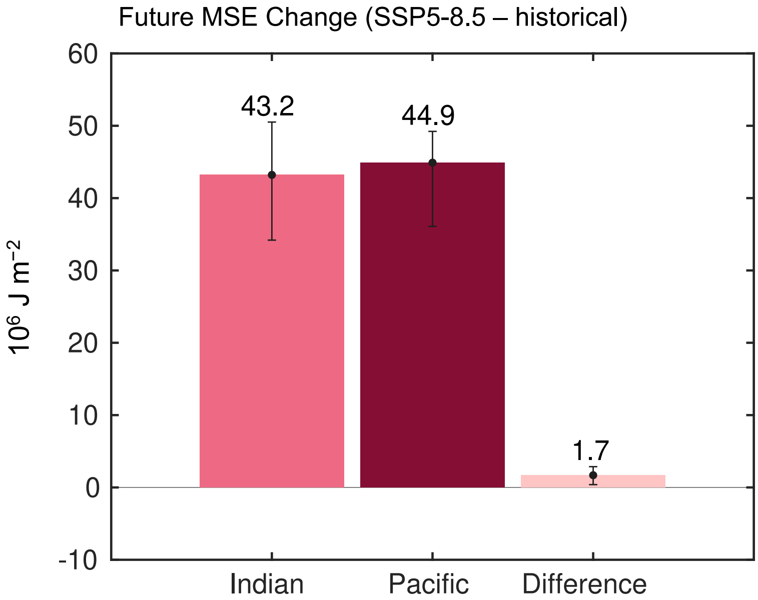

Supplementary Fig. 12. Indian versus Pacific Ocean MSE change in the high-end scenario. Bar plot of the projected change of the regional mean 1000–500-hPa MSE difference between SSP5-8.5 (2064–2099) and historical (1979–2014) scenarios in the tropical Indian (20°S–10°N, 50°–110°E) and Pacific Oceans (20°S–10°N, 110°E–150°W), and their difference when eliminating mean-state differences across the 12 good models. Error bars show the inter-model spread from the 25th to 75th percentile of the values output by the models.